Journal of ELECTRONIC MATERIALS
https://doi.org/10.1007/s11664-020-08071-4
© 2020 The Minerals, Metals & Materials Society

Measurement of Electric and Magnetic Properties of ZnO Nanoparticles in the X-Band Using Nicolson–Ross–Weir Analysis

KH. MABHOUTI,[1,3] M. KARAMIRAD,[2] P. NOROUZZADEH,[1] M.M. GOLZAN,[1] and R. NADERALI[1]

1.—Department of Physics, Faculty of Sciences, Urmia University, Urmia, Iran. 2.—Department of Electrical Engineering, Urmia University, Urmia, Iran. 3.—e-mail: kh.mabhouti@urmia.ac.ir

The electric and magnetic properties of zinc oxide (ZnO) nanoparticles (NPs) have been investigated through waveguide measurement in the x-band. Because of the advantages of the x-band, the application of the Nicolson–Ross–Weir (NRW) method was able to be used to extract the mentioned characteristics from the scattering parameters. The advantages of the NRW method are that it is fast and applicable to waveguides and coaxial lines, and it can also be used to determine both the permittivity and permeability. Therefore, the results show two main resonant frequencies at 9.279 GHz and 10.46 GHz. The response of the ZnO NPs for an incident electromagnetic wave implies that both capacitance and inductance behaviors can be observed. Finally, the obtained magnetic susceptibility characteristic confirms that the ZnO NPs are ferromagnetic over the frequency range from 8 GHz to 8.265 GHz and paramagnetic up to 12.5 GHz.

Key words: Zinc oxide nanoparticles, Nicolson–Ross–Weir method, scattering parameters, x-band, electric and magnetic properties

INTRODUCTION

X-band measurements have received much attention in the past due to some advantages such as low noise data communications and high-power capable antennas. Recent development in the x-band regarding such advantages has led to remarkable applications. Synthetic aperture radar (SAR), communications satellite, i.e., uplink, and remote sensing for monitoring weather conditions, so far have been promising applications of the x-band. However, further works must be performed to resolve its limitations. For this purpose, the realization of material behavior in the band is a vital issue.[1–4] Most recently, nanomaterials have received more attention in both theoretical and experimental fields as a developing research topic due to their small grain sizes, large grain boundaries, quantum size effects, and adequately large surface-to-volume ratio in comparison with their bulk form.[5] Oxide semiconductors have been widely used in a variety of fields such as solar cells,[6] sensors,[7] and electrical and optical devices[8] owing to their semiconducting and magnetic behaviors. Among the semiconductor nanomaterials, ZnO is inexpensive and important,[9,10] which makes it a promising material as an available candidate for electronics[11] and optoelectronics[12] including applications to solar cells,[13] light-emitting diodes,[14] and ultraviolet microlasers.[15] Moreover, ZnO is introduced as radiation hard and can be utilized for space-based electronics, where many types of radiation are rampant.[16] Different chemical route processes have been utilized to prepare ZnO NPs such as hydrothermal,[17] solvothermal,[18] co-precipitation,[19] microemulsion,[20] and sol–gel.[21] Compared with other techniques, the sol–gel route is popularly used for the synthesis of ZnO NPs because of its reliability, lower cost,

(Received September 21, 2019; accepted March 7, 2020)

Published online: 23 March 2020

environmentally friendly nature, and short time required for synthesis for industrial purposes, which provides rigorous control of the size and shape of the NPs.

This paper focuses on the electric and magnetic characteristics of the simple sol–gel-synthesized ZnO NPs in the x-band. For this purpose, the Nicolson–Ross–Weir (NRW) method has been employed to obtain the aforementioned properties. The utilized scattering parameters in the method have been obtained through waveguide (WR90) measurement using a network analyzer (Agilent E8363C). The disadvantages of the Fourier transform infrared (FTIR) method, such as low-resolution point (the number of results compared to the frequency steps) and main application in ultraviolet (UV) and visible regions, means that the above material properties are derived in low frequencies (Giga-hertz). Generally speaking, the empirically obtained scattering parameters (*S*-parameters) are used to obtain numeric electric and magnetic properties such as permittivity and permeability to characterize impedance. The results show that the ZnO NPs have a trade-off between capacitance and inductance behavior along with almost constant resistance. Furthermore, the paramagnetic and ferromagnetic properties of the ZnO NPs have been observed at the x-band of the electromagnetic spectrum.

EXPERIMENT

Sample Preparation

Pure ZnO nanoparticles (NPs) were synthesized using a simple sol–gel technique with highly pure zinc acetate dehydrate (ZAD) as a precursor, monoethanolamine (MEA) as a stabilizer, and 2-methoxy ethanol as a solvent. In this study, all the reagents were purchased from Merck, Germany, and used without any additional purification. For more detail of the synthesis, the preparation process of ZnO NPs is the same, which is comprehensively described in our earlier work.[22]

Measurements

The structural properties of the prepared sample are carried out using a high-resolution X-ray diffractometer (XRD) with Cu-Kα radiation at λ = 0.154056 nm (Philips PW 1730). The surface morphology is examined via field emission scanning electron microscopy (FE-SEM) (MIRA3, Tescan, Czech Republic).

Structural Analysis

XRD pattern of the synthesized ZnO is exhibited in Fig. 1. We can observe that the synthesized sample is in good agreement with JCPDS card No. 036-1451 wurtzite-type hexagonal structure, which verifies the constitution of the ZnO lattice in the synthesized sample. Also, the absence of any other

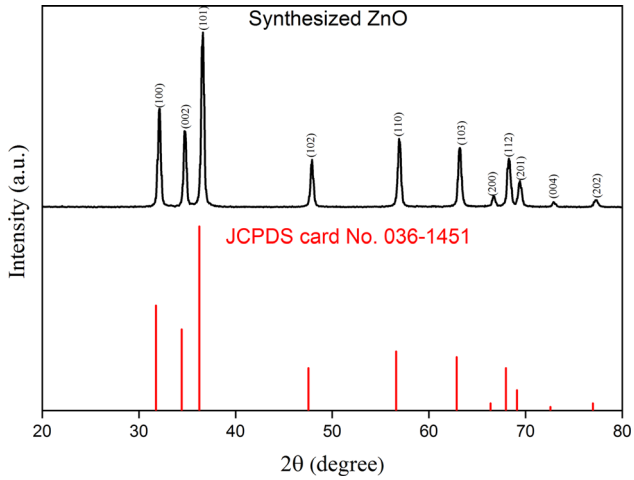

Fig. 1. XRD pattern of the synthesized ZnO nanopowder and the JCPDS card.

impurities peaks confirms the high purity of the sample. Furthermore, the presence of diffraction peaks at (100), (002), (101), (102), (110), (103), and (112) verifies the hexagonal wurtzite lattice structure of the sample. The lattice parameters (c and a) can be obtained from peaks at (002) and (100), respectively, allowing us to calculate the volume (V) of a hexagonal close-packed unit cell.[23,24] Table 1 presents the unit cell volume and lattice parameters calculated from the XRD data. As can be seen from Table 1, the unit cell volume and lattice parameters are similar to those obtained from the JCPDS card. However, in the compactness hcp phase, the c/a proportion is deviates a bit from JCPDS, which is related to the nanometric characteristics of the defects and crystallites. According to the literature,[25,26] the crystallite sizes have been investigated based on peak broadened utilizing X'Pert HighScore software. The mean crystallite diameters of the particles have been computed from the broadening of the peaks using the Debye–Scherrer equation:[27]

$$D = \frac{k\lambda}{\beta_{hkl}\cos\theta} \tag{1}$$

where θ is the corresponding Bragg angle, k equals 0.9, D is the crystallite diameter, β is the full width at half maximum (FWHM).[27] The obtained crystallite diameter value of the synthesized sample is about 26.76 nm.

Morphological Properties

The surface morphology of the prepared sample has been investigated by FE-SEM. The obtained FE-SEM image is depicted in Fig. 2. Digimizer software (version 4.1.1.0) has been used to examine the diameter of the particles. As shown in Fig. 2, the particle sizes are distributed randomly and have different sizes, ranging from 20 nm to 140 nm. The average particle size of 50 particles is approximately 70 nm (between 20 nm to 133 nm). The high-

Table 1. Lattice parameters and cell volume (V) of synthesized ZnO nanopowder

Samples	a (A)	c (A)	c/a	V (A^3)	Structure
JCPDS 36-1451	3.2498	5.2066	1.602	47.62	Hexagonal
Pure ZnO	3.2135	5.1587	1.605	46.13	Hexagonal

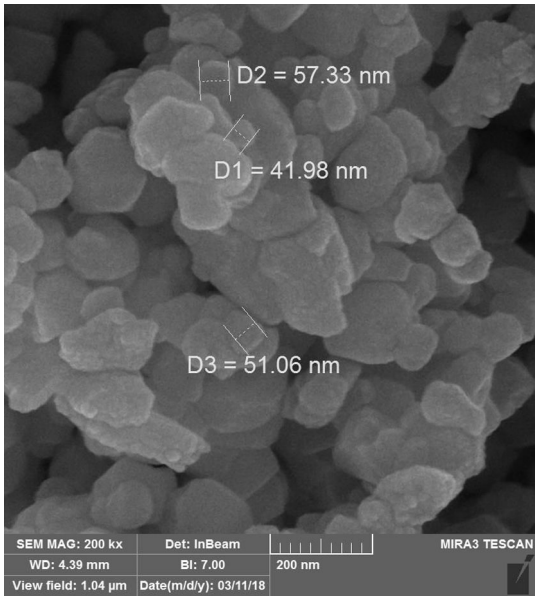

Fig. 2. FESEM image of the synthesized ZnO NPs.

resolution FE-SEM images show that the ZnO NPs appear in the form of a hexagonal structure. We can deduce that the grain sizes of the prepared sample are nanoscale, which is in proper compliance with the obtained particle size from XRD.

MEASUREMENT AND NRW METHOD

In this paper, the response of ZnO NPs with respect to electromagnetic waves in the range of 8 GHz to 12.5 GHz is investigated. To study the response of the nanoparticles to the incident waves, S-parameters must be defined. The parameter is represented as S_{ij}, in which the first subscript is referred to as the responding port (i), and the second one is referred to as the incident port (j). Besides, the S_{ij} is the ratio of the transmitted per reflected waves of the input port to the transmitted per reflected waves of the output port. In the complex parts (imaginary and real parts), the S-parameters are obtained for a given frequency and are described as frequency-dependent parameters. Through the results concerning the previous reported efforts, waveguide measurement is the most common. As stated in,[28] the waveguide measurement setup is employed to measure the transmission per reflection coefficients. Figure 3 illustrates the prototype of the fabricated ZnO NPs inside the sample holder of the standard WR90 waveguide with inner dimensions of $22.86 \times 10.16\ \text{mm}^2$ (see Fig. 3a) and the cut-off frequency of 6.557 GHz (the dominant TE10). As detailed in Fig. 3b and c, the proposed setup is connected to the network analyzer (Agilent E8363C). The measurement procedure has been carried out in two steps. In the first step, the limitation of the waveguide measurement is its inability to measure the phase variation on the surface of the ZnO NPs. Therefore, the calibration method (X11644A x-band module) was conducted on the waveguide setup to improve the results. Thus, the transmission per reflection coefficients was subsequently measured more confidently. It should be noted that the tangential electric field on the walls of the waveguides is equal to zero. Regarding the measurement process, an appropriate method is needed to derive the electric and magnetic properties of the ZnO NPs. According to the NRW method and multiple reflections theory,[29,30] the procedure of material characteristics extraction is based on S-parameters measured by the network analyzer (see Fig. 3b). Since the scattering parameters can be expressed as a function of the reflection and transmission coefficients at the interface of the two infinite media (air and sample), then:[30]

$$S_{11} = \frac{\Gamma(1 - T^2)}{1 - \Gamma^2 T^2} \tag{2a}$$

and

$$S_{21} = \frac{T(1 - \Gamma^2)}{1 - \Gamma^2 T^2} \tag{2b}$$

However, the reflection and transmission coefficients can be deduced as,

$$\Gamma = \chi \pm \sqrt{\chi^2 - 1} \tag{3}$$

where the parameter χ needs to be derived as a function of the S-parameters:

$$\chi = \frac{S_{11}^2 - S_{21}^2 + 1}{2S_{11}} \tag{4}$$

It is worth noting that the sign in Eq. (3) should be appropriately chosen to find the correct root. In order to delineate, the condition ($|\Gamma| < 1$) is considered throughout the paper. Taking advantage of the above equations, the permeability of the infinite sample in the waveguide environment with respect to Eq. (4) can be expressed as (5):

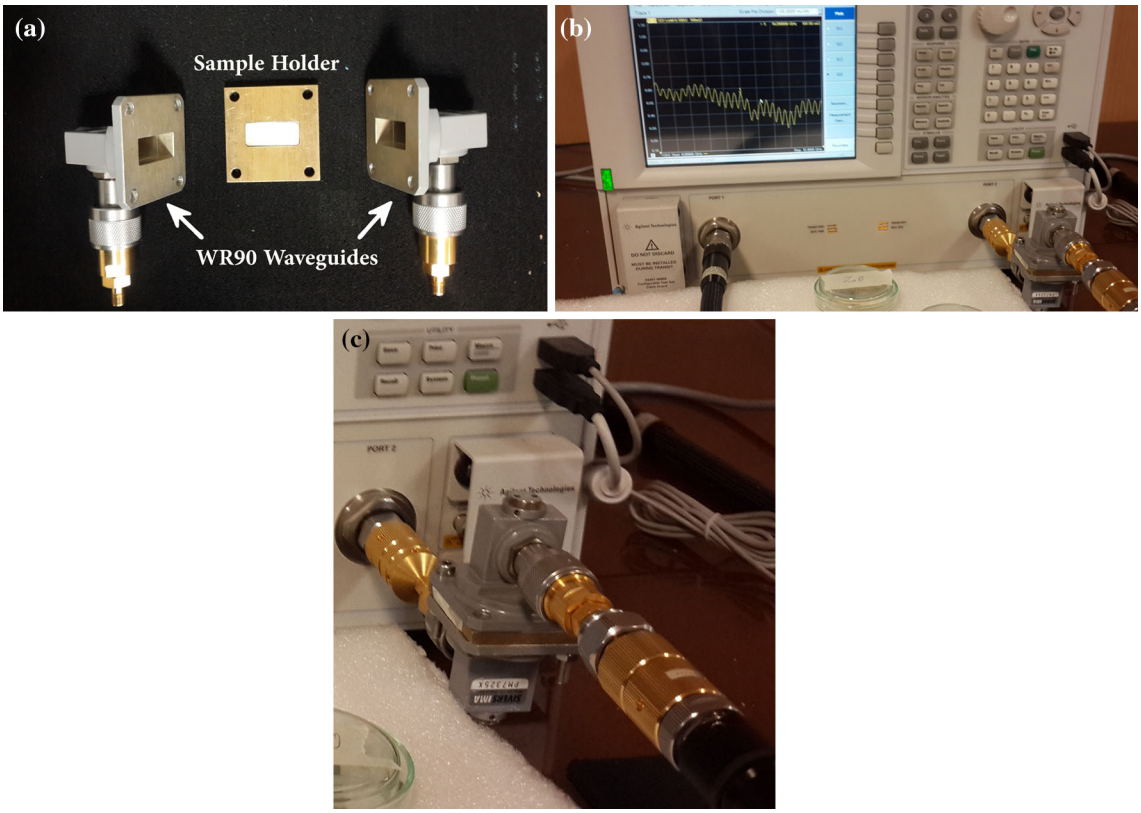

Fig. 3. The experimental setup for S-parameters measurements including an appropriate holder and standard WR90 waveguides (a), network analyzer (b), and enlarged waveguide setup (c).

$$\mu_r = \frac{1+\Gamma}{\Lambda(1-\Gamma)\sqrt{\frac{1}{\lambda_0^2}-\frac{1}{\lambda_c^2}}} \tag{5}$$

where λ_0 and λ_c are free-space wavelength and cut-off wavelength, respectively. The auxiliary parameters λ_g and Λ are defined as wavelength in the waveguide and normalized wavelength:

$$\Lambda = \frac{i2\pi l}{\ln\left(\left|\frac{1}{T}\right|\right) + i\left[\angle\left(\frac{1}{T}\right) + 2\pi n\right]}, \tag{6}$$

$$n = \text{integer}\left(\frac{l}{\lambda_g}\right), \quad \text{where } \lambda_g = \frac{\lambda_0}{\sqrt{1-\left(\frac{\lambda_0}{\lambda_c}\right)}}. \tag{7}$$

The symbol $\angle$ and l are the angle operator of the inverse transmission coefficient in each frequency and the length of the proposed sample. On the contrary, the permittivity is derived as a function of the derivation of the magnetic permeability:

$$\varepsilon_r = \frac{1}{\mu_r}\left(\frac{\lambda_0^2}{\Lambda^2} + \frac{\lambda_0^2}{\lambda_c^2}\right) \tag{8}$$

To gain a better understanding of the presented method, the summary flowchart is depicted in Fig. 4.

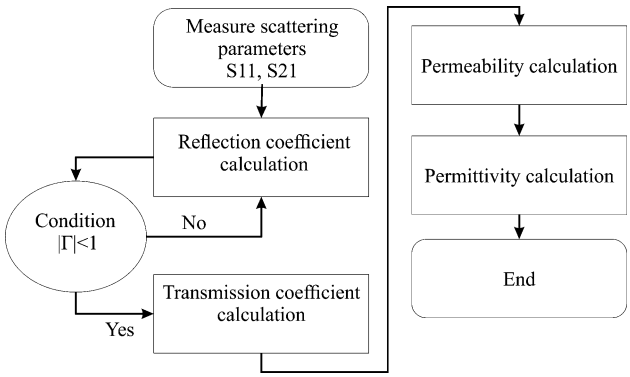

Fig. 4. Flowchart of the Nicholson–Ross–Weir (NRW) calculation method.

RESULTS AND DISCUSSION

Figure 5 shows the transmission ($S21$), reflections ($S11$), and absorption coefficients over the frequency range of 8–12.5 GHz. With respect to curve $S21$, the minimum value of the transmitted amplitude at 8 GHz is 29%, and its maximum at frequencies above 12.17 GHz is 60%. In the red dashed line curve, the minimum value for frequencies above 12.2 GHz is 26% and reaches 68% at 8 GHz. Two resonances are observed in this graph at frequencies 9.279 GHz and 10.46 GHz. It can be stated that with respect to these two resonant frequencies, the inductance and capacitance behavior of the material

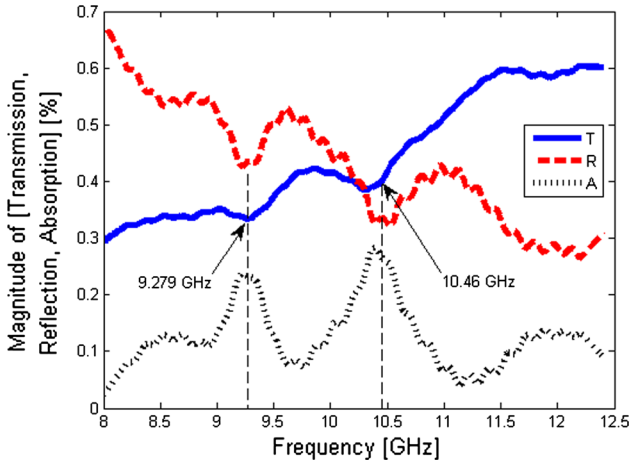

Fig. 5. Measured transmission (*T*, blue line), reflection (*R*, red dash line), and absorption rate (*A*, black dot line) of ZnO nanopowders at room temperature (Color figure online).

can be observed. The absorption rate is a parameter which is defined as the absorbed energy of the material in a specified frequency. It should be noted that absorptivity A is expressed as:[28]

$$A = 1 - R - T = 1 - |S_{11}|^2 - |S_{21}|^2 \qquad (9)$$

where R and T refer to the reflected and transmitted power, respectively. As shown in Fig. 5, the absorption coefficient is about 23% and 28% for the two mentioned resonant frequencies. Figure 6 depicts the real and imaginary parts of $(\varepsilon = \varepsilon' - j\varepsilon'')$ and $(\mu = \mu' - j\mu'')$ variations respect to frequency. Complex permittivity (ε) and complex permeability (μ) are crucial factors used to determine the microwave absorption characteristics of an absorber where the real parts of complex permeability (μ') and complex permittivity (ε') demonstrate the storage potentiality of magnetic and electric energy and the imaginary parts $(\varepsilon''$ and $\mu'')$ explain the loss potentiality of the magnetic and electric energy.[31] In Fig. 6a, ε' is negative at the frequency range of 8–8.247 GHz. This indicates that there is no feasibility of propagating the electric field of the electromagnetic wave inside the material. By increasing the frequency of about 8.247 GHz, the real ε reaches positive values, and therefore, it sharply increases in a frequency range of 8.247–8.46 GHz, leading to a fluctuation around 3. The imaginary part of the permittivity is always negative, and it shows that the material does not impose a loss on the input field. The real part of μ is reduced at a frequency range of 8–8.459 GHz. As the frequency increases, it then fluctuates around a value of 1.5 (see Fig. 6b). The ZnO NPs represent a magnetic loss in the range of 8–8.185 GHz, released from the magnetic loss conditions by increasing the frequency. The measured ε and μ lead to drive other electric and magnetic parameters. For this purpose, impedance characteristic $(Z = R - jX)$ is a main parameter used to determine the resistance (R), capacitance and

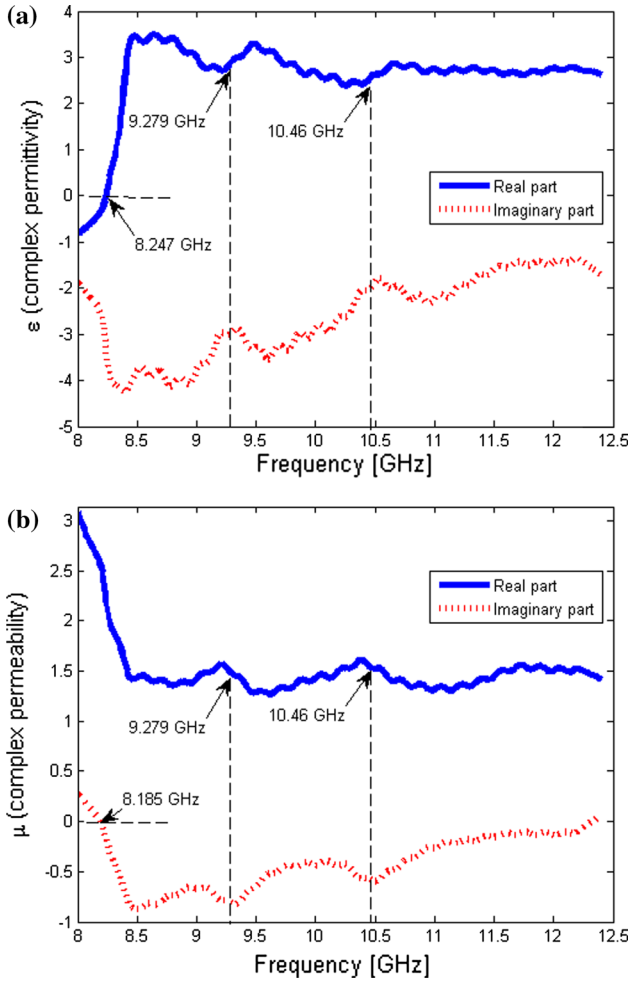

Fig. 6. Measured real part (blue line) and imaginary part (red dot line) of the complex permittivity (a) and permeability (b) (Color figure online).

reactance (X) of the ZnO NPs. In order to extract the impedance characteristic, the following equation is applied:

$$Z = \eta_0 \sqrt{\frac{\mu}{\varepsilon}} \qquad (10)$$

where $\eta_0 (= 377\Omega)$ is the impedance characteristic of the air. Figure 7 exhibits the imaginary and real parts of the impedance characteristic, which is normalized to η_0. As can be seen, the imaginary part of the impedance shows a sharp drop in the range of 8–8.494 GHz. After that, its value varies by about 0.1. The real part of the impedance increases slightly at two resonant frequencies of 9.279 GHz and 10.46 GHz, and afterward, its value varies by about 0.6. In the range of the two resonant frequencies, the variations in the real and imaginary impedance are conversely changed.

Initially, ZnO NPs experience alteration in the dipole polarization orientation through the external electromagnetic field, which produces surface polar charges. The presence of the polarized charges at the surface results in distribution of surface

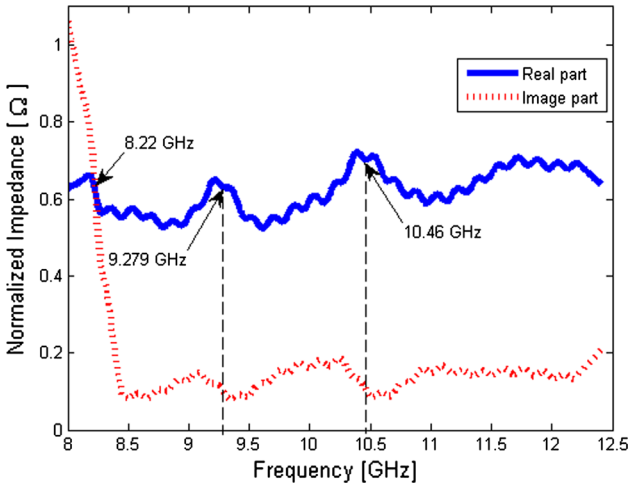

Fig. 7. Variation of the real part (blue line) and imaginary part (red dot line) of the normalized complex impedance with frequency (Color figure online).

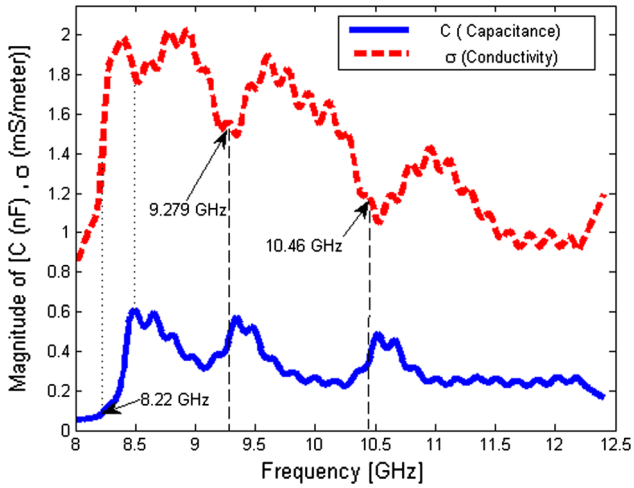

Fig. 8. Frequency dependence of capacitance (blue line) and conductivity (red dashed line) at room temperature (Color figure online).

currents. According to Faraday's induction law, the material reacts to the production of sudden surface currents. When this happens, the ZnO NPs acts as an inductor, which opposes the changes in initial flux with respect to the Lenz law. As a result, the real part of permittivity is negative at the beginning. In this paper, the measurements are carried out with a constant intensity and frequency variation of the electromagnetic field ($\overrightarrow{E_i} = \vec{E}_0 e^{-j\beta}$, $\left|\vec{E}_0\right|$ = constant). As is known, the field fluctuation period is inversely proportional to the frequency, which means that the field is applied in shorter periods to the ZnO NPs. In consequence, the ZnO NPs have a shorter time to respond to the external field and alter the orientation of dipole polarization. The increasing frequency consequently causes the arrangement of the orientation of the polarization, the surface polarized charges, and surface currents to be disturbed and decreased. Therefore, the density of the electric charges condensed within the NPs, and the inductance would be decreased. The maximum inductive value of the matter is in the range of 8–8.22 GHz, and the imaginary part of the impedance is abruptly reduced over the presented frequency range. The electric charge accumulation characterizes the capacitance condition. The inductance behavior decreases equal to the increase of the amount of stored electromagnetic wave energy in the NPs, and simultaneously, increases in the capacitance behavior. This increase implies that ε' is positive, and the propagation conditions of the electrical component of the electromagnetic wave are facilitated. Compared to the surface currents generated by the induction of electromagnetic waves on the ZnO NPs, the electrical resistance (R) is almost constant.

Figure 8 shows the capacitance (blue line curve) and conductivity (red dash curve) of the material versus frequency. The relationship between capacitance and conductivity with imaginary parts of Z and ε are as follows:[32]

$$C = \frac{1}{2\pi f Z''} \tag{11a}$$

$$\sigma = \varepsilon_0 \varepsilon'' \omega \tag{11b}$$

As can be seen, the capacitance of the ZnO NPs has initially been low. The capacitance increases abruptly to its maximum value (0.6055 nF at 8.494 GHz) and then decreases to 0.3121 nF at 9.085 GHz. Similarly, this increase is observed at the two mentioned resonant frequencies but is not as large as the maximum value at 8.494 GHz. As can be seen in Fig. 8, the greater the increase in capacitance value, the less the decrease in conductivity. As stated, the two minimum values of 1.556 mS/m and 1.169 mS/m are observed at the two respective frequencies of 9.279 GHz and 10.46 GHz.

The incident of the electromagnetic wave in a period of time is attempted to reduce the above-defined capacitance at the specified frequency range. It is implied that the dipoles cannot attain the previous orientation and have a shorter time interval to modify and rotate the polarization. Based on Fig. 5, the two resonances are measured at frequencies of 9.279 GHz and 10.46 GHz. In two resonant frequencies, since the wavelength is proportional to the dimensions, the density of the electrical charges in the two bulky portions of the ZnO NPs is enhanced. Consequently, an increase in capacitance is observed for each of the resonant frequencies. It is noted that the absorption rate is also increasing at these two frequencies. As shown in Fig. 8, the required transient response time ($\tau = RC$) for full charge is 48.74, 50.36, and 49.16 μs for frequencies of 8.499 GHz, 9.34 GHz, and 10.52 GHz, respectively.

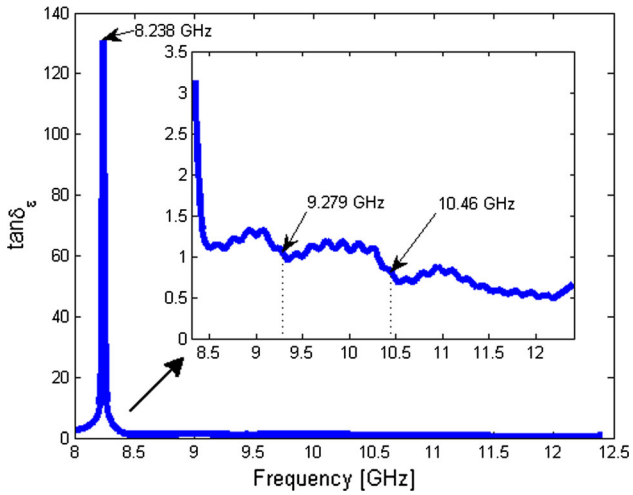

Fig. 9. The dielectric loss tangent (tan δ_ε) versus frequency at room temperature.

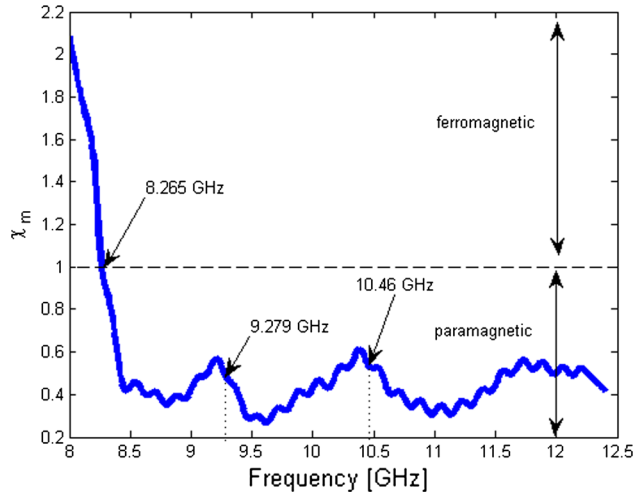

Fig. 10. Frequency dependence of magnetic susceptibility (χ_m) at room temperature.

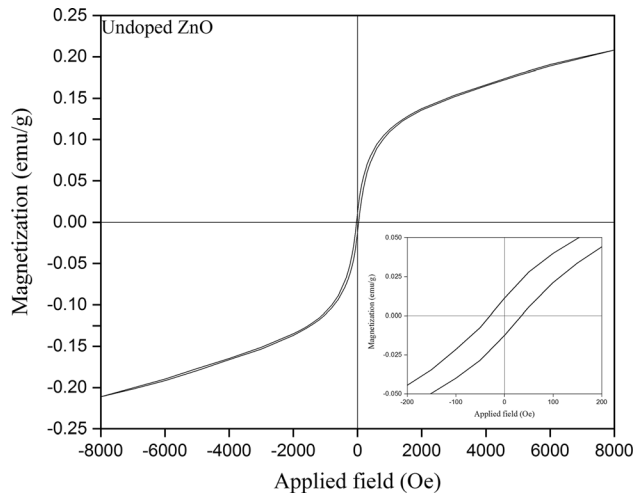

Fig. 11. Measured magnetization at the room temperature for undoped ZnO.

To characterize dielectric loss capability, the dielectric loss tangent ($\tan\delta_e = \frac{\varepsilon''}{\varepsilon'}$) is commonly used; moreover, it affirms that the loss of electric energy at the interval of 8–12.5 GHz is very high. Since the dielectric loss behavior is chiefly related to the polarization and conductivity loss,[33] and the polarization loss can contain the dipole orientation polarization, electronic polarization, ionic polarization, and interfacial polarization (polarization of space charge).[34] Therefore, from the comparison of the conductivity and dielectric loss on Figs. 8 and 9, it can be deduced that in ZnO NPs, for the attenuation of incident electromagnetic waves, the conductivity loss is the only way to create a dielectric loss. Figure 9 shows the loss tangent versus frequency. As shown, the highest value of $\tan\delta_e$ is pinpointed at a frequency of 8.238 GHz, and for larger frequencies, its value is reduced to about 1. For the two aforementioned resonant frequencies, the values of loss tangent are 1.056 and 0.7833, respectively. Therefore, at higher frequencies ($f \geq 11.49$GHz), the decrease continues to about 0.5. We further analyze the magnetic susceptibility as a material magnetization characteristic in an imposed electromagnetic wave (see Fig. 10). It can be found that the ZnO NPs are paramagnetic and ferromagnetic at frequencies lower and higher than 8.265, respectively. As can be seen from Figs. 6 and 7, the maximum value of susceptibility is in the frequency range of 8–8.265 GHz, which is verified by Fig. 10.

Figure 11 demonstrates the measured magnetization of the undoped ZnO sample, which is performed using a vibrating-sample magnetometer (VSM) with an applied magnetic field at room temperature. As can be seen, a weak ferromagnetic and chiefly a paramagnetic signal are detected from the M-H loop confirming the obtained results in Fig. 10. A small value of coercivity implies the presence of hysteresis in the sample, which can be attributed to the localized electron spin moments or exchange interactions attributed to the zinc interstitials (Zni) and oxygen vacancies (Vo) at the surface of NPs or intrinsic defects in NPs.[35,36] As reported in our previous work,[22] the crystallite size of the synthesized undoped ZnO particles is determined using ImageJ and Digimizer 4.1.1.0[37,38] software. The results show that all the particles are in the nanoscale range of 20 nm to 130 nm, with an average of approximately 70 nm. According to the literature[39–41] and based on the core–shell model, contrary to bulk form, it is expected to observe two resonances in the x-band for ZnO when the average crystallite size is about 50 nm. Figure 12 shows that the magnetic loss factor, ($\tan\delta_m = \frac{\mu''}{\mu'}$), first increases, and then decreases by increasing the microwave frequency. In general, the magnetic loss is derived from eddy-current loss, magnetic hysteresis loss and residual loss.[42] The eddy-current loss can be expressed as:[43]

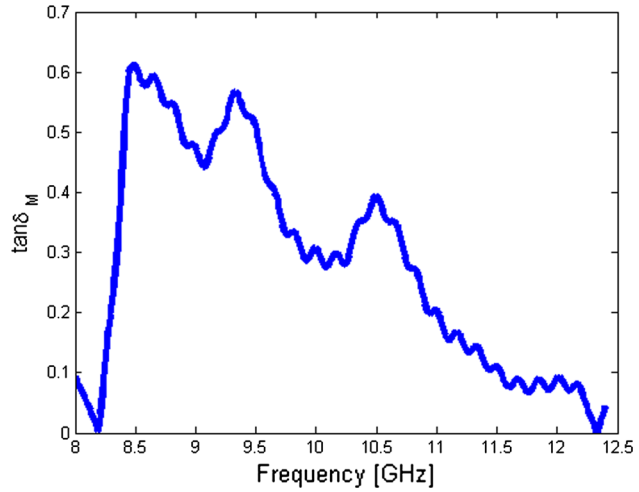

Fig. 12. The magnetic loss tangent ($\tan\delta_m$) versus frequency at room temperature.

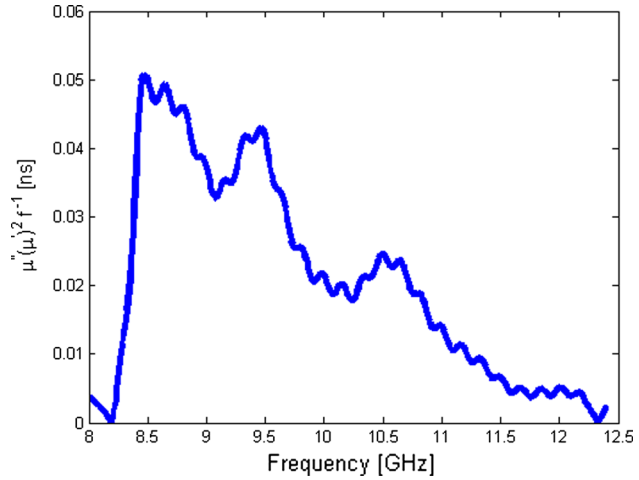

Fig. 13. Eddy-current ($\mu''(\mu'^{-2})f^{-1}$) variation response over the frequency at room temperature.

$$\mu''(\mu'^{-2})f^{-1} = 2\pi\mu_0 d^2\sigma \qquad (12)$$

where μ_0 is the space permeability, d is the thickness and σ is the conductivity. The values of $\mu''(\mu'^{-2})f^{-1}$ are depicted in Fig. 13. Accordingly, the eddy-current is ineffective to magnetic loss due to the values of the $\mu''(\mu'^{-2})f^{-1}$ should be constant, but decrease with increasing frequency.[44,45] As illustrated in Fig. 12, magnetic hysteresis loss may occur in the undoped ZnO. As mentioned above, the NPs size and shape can lead to generating dielectric resonances and magnetic loss, respectively.[40,42,46]

CONCLUSION

Nanostructured ZnO possesses electric and magnetic properties subject to an incident electromagnetic wave over the x-band. The proposed characteristics are derived through the reflection coefficient condition ($|\Gamma|<1$) in the NRW method, which improves the results. The measurement procedure is carried out with a high-resolution point of view. Accordingly, the most important error is instrument noise, including low noise and phase noise caused by a source inside the test set. To reduce this noise, increasing the power source is helpful. Because there is a limitation in providing power, other methods should be employed for noise reduction. In order to eliminate the systematic error, calibration methods are employed using equations known as the error model. Following this, the calibration method utilized in the test set is the Thru-Reflect-Line (TRL) method, whose accuracy is high to eliminate the noise.[47] Therefore, the results realized from the test set are expected to be improved. Contrary to other literature,[48–50] the measurement procedure with a high resolution leads to obtaining the main resonant frequencies. In this paper, two main resonant frequencies are extracted from the experimentally scattering parameter responses. Moreover, the microwave absorption varies from a different concentration of NP in composites. Furthermore, this study shows that the reflection coefficients are 43% (− 6.30 dB) and 33% (− 9.25 dB) at the resonance frequencies resulting in absorption rates reach 23% and 28%, which contradicts the literature.[46,51] According to the results, the equivalent circuit of the ZnO NPs will include inductance along with the mentioned capacitance and resistance in.[52] The dominant induction behavior is observed at low frequencies. Then, as the frequency increases, the capacitance behavior attempts to attain higher values compared to the initial cases. Afterward, the resistance increases with a slight slope over the same frequency range.

ACKNOWLEDGMENTS

The authors thank the Northwest Antenna and Microwave Research Laboratory (NAMRL) for their beneficial and professional help. Thanks are also due to Prof. Changiz Ghobadi, who has given us much valuable advice in the stages of this work. We also thank Mr. Barzegari for his ongoing collaboration with our experimental work.

REFERENCES

1. S. Kumar, P. Kumar, N. Singh, and V. Verma, *J. Magn. Magn. Mater.* 488, 165364 (2019).
2. Z. Li, A. Haigh, C. Soutis, and A. Gibson, *Compos. Struct.* 208, 224 (2019).
3. R. Singh, S. Bahel, and S.B. Narang, *J. Alloys Compd.* 784, 668 (2019).
4. R. Shu, W. Li, Y. Wu, J. Zhang, and G. Zhang, *Chem. Eng. J.* 362, 513 (2019).
5. M.K. Gupta, N. Sinha, and B. Kumar, *J. Appl. Phys.* 112, 14303 (2012).
6. Z.-S. Wang, C.-H. Huang, Y.-Y. Huang, Y.-J. Hou, P.-H. Xie, B.-W. Zhang, and H.-M. Cheng, *Chem. Mater.* 13, 678 (2001).
7. B.P. Seung and C.K. Yun, *J. Aerosol Sci.* 1001, S473 (1997).

8. S.T. Kochuveedu, Y.H. Jang, and D.H. Kim, *Chem. Soc. Rev.* 42, 8467 (2013).
9. M. Wang, S.H. Hahn, E.J. Kim, J.S. Kim, S. Kim, C. Park, and K.-K. Koo, *Thin Solid Films* 516, 8599 (2008).
10. Ü. Özgür, Y.I. Alivov, C. Liu, A. Teke, M.A. Reshchikov, S. Doğan, V. Avrutin, S.-J. Cho, and H. Morkoç, *J. Appl. Phys.* 98, 11 (2005).
11. K. Sivaramakrishnan and T.L. Alford, *Appl. Phys. Lett.* 94, 52104 (2009).
12. A.B. Djurišić, A.M.C. Ng, and X.Y. Chen, *Prog. Quantum Electron.* 34, 191 (2010).
13. A. Nuruddin and J.R. Abelson, *Thin Solid Films* 394, 48 (2001).
14. J. Kong, S. Chu, M. Olmedo, L. Li, Z. Yang, and J. Liu, *Appl. Phys. Lett.* 93, 132113 (2008).
15. Z.K. Tang, G.K.L. Wong, P. Yu, M. Kawasaki, A. Ohtomo, H. Koinuma, and Y. Segawa, *Appl. Phys. Lett.* 72, 3270 (1998).
16. U. Pal, R. Melendrez, V. Chernov, and M. Barboza-Flores, *Appl. Phys. Lett.* 89, 183118 (2006).
17. S. Gao, D. Li, Y. Li, X. Lv, J. Wang, H. Li, Q. Yu, F. Guo, and L. Zhao, *J. Alloys Compd.* 539, 200 (2012).
18. Z. Liu, Q. Zhang, G. Shi, Y. Li, and H. Wang, *J. Magn. Magn. Mater.* 323, 1022 (2011).
19. G. Vijayaprasath, R. Murugan, T. Mahalingam, and G. Ravi, *J. Mater. Sci.: Mater. Electron.* 26, 7205 (2015).
20. Ö.A. Yıldırım and C. Durucan, *J. Alloys Compd.* 506, 944 (2010).
21. M. Arshad, A. Azam, A.S. Ahmed, S. Mollah, and A.H. Naqvi, *J. Alloys Compd.* 509, 8378 (2011).
22. P. Norouzzadeh, K. Mabhouti, M.M. Golzan, and R. Naderali, *J. Mater. Sci. Mater. Electron.* 1, 1 (2019).
23. N. Fifere, A. Airinei, D. Timpu, A. Rotaru, L. Sacarescu, and L. Ursu, *J. Alloys Compd.* 757, 60 (2018).
24. P. Kumar, A.K. Yadav, A.G. Joshi, D. Bhattacharyya, S.N. Jha, and P.C. Pandey, *Mater. Charact.* 142, 593 (2018).
25. A.H. Bahrami, H. Ghayour, and S. Sharafi, *Powder Technol.* 249, 7 (2013).
26. S.O. Gashti, A. Fattah-Alhosseini, Y. Mazaheri, and M.K. Keshavarz, *J. Alloys Compd.* 688, 44 (2016).
27. T. Debnath, P. Saha, N. Patra, S. Das, and S. Sutradhar, *J. Appl. Phys.* 123, 194101 (2018).
28. Y. Dong, P. Liu, D. Yu, G. Li, and L. Yang, *IEEE Antennas Wirel. Propag. Lett.* 16, 1115 (2016).
29. A.M. Nicolson, G.F. Ross, and I.E.E.E. Trans, *Instrum. Meas.* 19, 377 (1970).
30. W.B. Weir, *Proc. IEEE* 62, 33 (1974).
31. Y. Du, W. Liu, R. Qiang, Y. Wang, X. Han, J. Ma, P. Xu, and A.C.S. Appl, *Mater. Interfaces* 6, 12997 (2014).
32. H.M. Chenari, A. Hassanzadeh, M.M. Golzan, H. Sedghi, and M. Talebian, *Curr. Appl. Phys.* 11, 409 (2011).
33. B. Wen, M.-S. Cao, Z.-L. Hou, W.-L. Song, L. Zhang, M.-M. Lu, H.-B. Jin, X.-Y. Fang, W.-Z. Wang, and J. Yuan, *Carbon N. Y.* 65, 124 (2013).
34. C. Tian, Y. Du, P. Xu, R. Qiang, Y. Wang, D. Ding, J. Xue, J. Ma, H. Zhao, X. Han, and A.C.S. Appl, *Mater. Interfaces* 7, 20090 (2015).
35. A. Sundaresan, R. Bhargavi, N. Rangarajan, U. Siddesh, and C.N.R. Rao, *Phys. Rev. B* 74, 161306 (2006).
36. D. Guruvammal, S. Selvaraj, and S.M. Sundar, *J. Alloys Compd.* 682, 850 (2016).
37. P. Shukla and J.K. Shukla, *J. Supercond. Nov. Magn.* 32, 721 (2019).
38. P. Norouzzadeh, K. Mabhouti, M.M. Golzan, and R. Naderali, *Optik* 204, 164227 (2020).
39. P. Jakes and E. Erdem, *Phys. Status Solidi (RRL)–Rapid Res. Lett.* 5, 56 (2011).
40. E. Erdem, *J. Alloys Compd.* 605, 34 (2014).
41. K. Zhang, F. Wu, Y. Jiao, M. Sun, Y. Xia, and A. Xie, *J. Mater. Chem. C* 7, 3590 (2019).
42. X. Huang, M. Zhang, Y. Qin, and Y. Chen, *Ceram. Int.* 45, 7789 (2019).
43. M. Wu, Y.D. Zhang, S. Hui, T.D. Xiao, S. Ge, W.A. Hines, J.I. Budnick, and G.W. Taylor, *Appl. Phys. Lett.* 80, 4404 (2002).
44. G.-S. Wang, Y.-Y. Wu, X.-J. Zhang, Y. Li, L. Guo, and M.-S. Cao, *J. Mater. Chem. A* 2, 8644 (2014).
45. Q. Liu, Q. Cao, H. Bi, C. Liang, K. Yuan, W. She, Y. Yang, and R. Che, *Adv. Mater.* 28, 486 (2016).
46. X.G. Liu, J.J. Jiang, D.Y. Geng, B.Q. Li, Z. Han, W. Liu, and Z.D. Zhang, *Appl. Phys. Lett.* 94, 53119 (2009).
47. R.B. Marks, *IEEE Trans. Microw. Theory Tech.* 39, 1205 (1991).
48. I. Sadiq, S. Naseem, M.N. Ashiq, M.A. Khan, S. Niaz, and M.U. Rana, *J. Magn. Magn. Mater.* 401, 63 (2016).
49. I. Sadiq, S. Naseem, S. Riaz, S.S. Hussain, H.M. Khan, M.N. Ashiq, and M. Rana, *J. Alloys Compd.* 715, 284 (2017).
50. I. Sadiq, S. Naseem, S. Riaz, S.S. Hussain, M.N. Ashiq, and M. Rana, *Prog. Nat. Sci. Mater. Int.* 28, 478 (2018).
51. Y.J. Chen, M.S. Cao, T.H. Wang, and Q. Wan, *Appl. Phys. Lett.* 84, 3367 (2004).
52. K. Omri, I. Najeh, and L. El Mir, *Ceram. Int.* 42, 8940 (2016).

Publisher's Note Springer Nature remains neutral with regard to jurisdictional claims in published maps and institutional affiliations.